



Selective laser melting of H13 tool steel powder: effect of process parameter on complex part production

F. Impaziente¹ · L. Giorleo² · F. Mazzucato¹

Received: 7 May 2022 / Accepted: 26 August 2023
© The Author(s) 2023

Abstract

This research work presents the investigation of H13 tool steel powder in the production of parts characterized by complex features via selective laser melting. The authors proposed a benchmark geometry with 40 mm nominal height, self-supported overhanging structure and internal channels. To investigate powder printability and process capabilities, an experimental campaign was designed as a function of laser power, scan speed and hatching distance. Full dense parts exhibiting 99.92% internal density have been achieved by imposing a laser power equal to 150 W, a scan speed equal to 500 mm/s and a hatching distance equal to 120 μm , while high geometrical accuracy in terms of no material drops along sample edges and low-dimensional deviations of the realized sloping surfaces (i.e., $+0.23^\circ$ and -0.90° for nominal 35° and 40° overhang, respectively) has been achieved for 150 W, 1000 mm/s, and 100 μm . Findings open the way to use SLM technology in the design of advanced cutting tool solutions.

Keywords Selective laser melting · Tool steel · Design for additive manufacturing

1 Introduction

The technological need for designing advanced cutting tool solutions exhibiting longer working life in conjunction with improved wear resistance and high-precision material removal is driving the industry to explore new cost-effective manufacturing solutions enabling the production of highly complex cutting tools exhibiting enhanced performance. Selective laser melting (SLM) is a powder bed fusion (PBF) technique capable to fabricate high-density metal parts with high-complex geometrical designs impossible to reach by means of conventional technologies [1–4]. Recently, industrial and academic efforts have focused on characterizing the processability of H13 steel powder through SLM for the

design and manufacturing of complex-shaped cutting tool solutions [5–9].

Several research works have analyzed the influence of SLM process parameters [10–13], raster patterns [14], preheating [15] and post-tempering treatments [16] on the final density, residual stress, and microstructure of SLM-fabricated high-carbon steel components. Laakso et al. [10] assessed the influence of the laser power (100–300 W), scan speed (400–1200 mm/s), and hatching distance (90–150 μm) on the final structural quality of H13 components, achieving notable results in terms of part porosity (up to 99%) for a power of 200 W, a scan speed of 1200 mm/s and a hatching distance lower than 120 μm . A similar analysis was designed by Fonseca et al. [11] where a parameter set for minimal linear crack density, minimal porosity and maximum density was found setting a laser power of 172 W, a scan speed of 700 mm/s and hatching distance equal to 80 μm . Acceptable mechanical properties were achieved by Katancik et al. [12] by means of SLM process optimization, observing a final density, microstructure, and microhardness of the as-fabricated H13 comparable to those of formed H13 tool steel parts. Yan et al. [13] focused their analysis on the residual stress of manufactured samples produced with a laser power of 150 W, a scan speed of 300 mm/s and a hatch spacing of 50 μm , finding values in a range between 940 and

✉ F. Impaziente
francesco.impaziente@supsi.ch

¹ Automation, Robotics and Machines Laboratory, Department of Innovative Technologies, ISTEPS, University of Applied Sciences and Arts of Southern Switzerland (SUPSI), Lugano-Viganello, Switzerland

² Advanced Laboratory Prototyping, Department of Industrial and Mechanical Engineer, University of Brescia, Brescia, Italy

1420 MPa. The authors concluded that the main reason for the high detected compressive residual stresses was the martensitic transformation that occurred during the SLM of the H13 steel. To reduce part porosity, Kurzynowski et al. [14] tested different scan strategies demonstrating that a proper selection of the chessboard strategy with small dimensions of individual fields prevented the influence of the size of the scan section on the relative density of the manufactured parts. A structured experimental campaign for the SLM of H13 employing 200 °C substrate preheating was performed by Narvan et al. [15], demonstrating that application of the preheating process not only enhances the relative density (99.7%) but also helps in eliminating the thermally induced cracks. Building upon these studies, the common processing defects in SLM have been classified by considering all contributing factors, for process monitoring and control purpose [17]. In addition, numerical models have been developed to enhance understanding of the multi-physics involved in the process [18].

Despite the remarkable results obtained from the above studies, the performed analyses mainly focus on the final quality of H13 simple-shaped geometries (e.g., cubes) without considering the influence of the main SLM process parameters on both the structural integrity and geometrical accuracy of geometrically complex H13 parts. Specifically, for highly complex geometrical designs where support structures cannot be placed due to accessibility constraints imposed by part's functionalities (e.g., conformal channels), the SLM process has to be optimized to ensure a defect-free and geometrically sound realization of the self-support features. Such process optimization often requires the implementation of different combinations of process parameters for the manufacturing of a single component, depending on the design complexity and geometrical features to be realized. In addition, all the cited studies report the manufacturing of samples with maximum heights of about 10 mm, neglecting the influence of the build height on the final quality of the as-built components (i.e., the effect of the increasing distance from the heated plate, discussed in [19, 20] for different materials). To the best of the authors' knowledge, few efforts have been currently performed to address the fabrication of complex H13 shapes taking into account process, material, and design constraints [21–28], missing in design rules driving the SLM process optimization of functionally shaped cutting tools for relevant industrial applications.

This research work focuses on the influence of the main SLM process parameters (i.e., laser power, scan speed, and hatching distance) on both the achievable geometrical accuracy and final structural quality of as-built geometrically complex H13 specimens. The 3D bulk geometries were designed to exhibit self-supporting features based on the design of a milling sleeve previously optimized for AM [23]. The main experimental results showed that

the manufacturing of high-quality H13 parts needs an adaptation of the SLM process parameters based on the geometrical complexity of the part design. The achieved experimental outcomes encourage the employment of combinations of SLM process parameters involving low laser power (i.e., 150 W) and medium–low volumetric energy densities (i.e., 80 J/mm³). Section 2 introduces the experimental equipment employed for sample manufacturing and the followed experimental methodology. Sections 3 and 4 deal with the achieved results and discussion, respectively. Finally, the main conclusions are discussed in Sect. 5.

2 Materials and methods

2.1 Materials and bulk geometry design

The metal powder used for sample manufacturing was AISI H13 powder (provider: Kind Special Alloy, Collegno, Italy). The particle size distribution was evaluated according to ASTM B822-20 standard [29] while the chemical composition was estimated through combustion analytical technique and inductively plasma optical emission according to ASTM E1019-18 and ASTM E1479-16 standard [30, 31]. Tables 1 and 2 report particle size distribution and chemical composition of the involved metal powder.

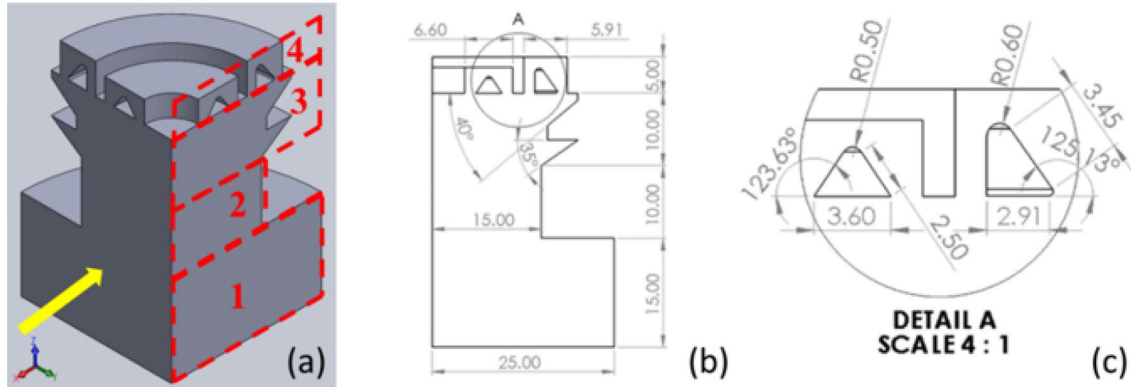
The bulk sample geometry was engineered considering the maximum height and the geometrical complexity of the milling tool presented by the authors in [23] (see Fig. 1). Specifically, the sample design was divided in four zones with the goal to analyze the influence of geometrical complexity on the structural integrity of the part (see Fig. 1a). Zone 1 aimed to analyze the effect of process parameters on the structural quality of the realized sample avoiding any issue related to part geometry; zone 2 meant to study the effect of an increasing distance from the heated plate in conjunction with a reduced layer size; in zones 3 and 4, the capability of the SLM process to generate self-supporting H13 structures was tested. Zone 3 was characterized by the presence of two overhanging surfaces with different slopes (35° and 40°—see Fig. 1b), whereas in zone 4, two different internal channels with different sizes and cross-sections were placed (i.e., an isosceles triangle cross-section and a rectangular triangle cross-section—see Fig. 1c).

Table 1 Particle size distribution according to ASTM B822-20 [μm]

D10	D50	D90
23.5	35.7	53.9

Table 2 Chemical composition according to ASTM E1019-18 and ASTM E1479-16 [%]

Element	C	S	Cr	Mn	Mo	P	Si	V	Fe
Min	0.35	0	4.8	0.25	1.2	0	0.8	0.85	bal
Results	0.38	0.004	5.0	0.38	1.24	0.016	0.9	0.89	
Max	0.42	0.02	5.5	0.5	1.5	0.03	1.2	1.15	


Fig. 1 a Bulk sample design concept: part geometry in 3D [mm]; b XZ cross-section [mm]; c XZ cross-section in zone 4 [mm]

2.2 SLM machine and experimental campaign design

The SLM system used for sample manufacturing was a Printsharp 250 (supplier: Prima Additive, Turin, Italy). The machine was equipped with an Yb laser with an emission wavelength ranging between 1060 and 1080 nm and a maximum power of 500 W on a focused 70 μm beam diameter. The SLM process was performed in an Argon inert building environment, ensuring an O_2 level of less than 500 ppm for all the AM process duration. To evacuate the smoke generated during the process and shield the f- Θ lens and laser optics, a 20 l/min Argon gas flow homogeneously distributed above the powder bed was used during sample manufacturing. The gas flow moved following the path indicated by the green arrows in Fig. 2a and was previously optimized to maximize smoke evacuation without blowing away the deposited powder bed.

To characterize the effect of the SLM process parameters on the final quality of H13 samples, an experimental campaign consisting of 3 input variables (i.e., P, v, h) and 3 levels each was designed, considering a volumetric energy density (VED) ranging between 42 to 250 J/mm^3 (see Table 3). VED is defined as

$$\text{VED} = \frac{P}{v \cdot h \cdot t}$$

where P is the laser power (W), v is the scan speed (mm/s), h is the hatching distance (μm) and t is the layer thickness

(μm). To explore the variable space correlated to the chosen energy range, P was set at 150, 225, and 350 W, v was set at 500, 750, and 1000 mm/s, and h was set at 80, 100, and 200 μm . Three repetitions for each combination of process parameters were executed, whereas t was kept constant at 30 μm . Table 3 summarizes the process variables and the VED calculated for each experimental combination. Another pivotal parameter involved in the SLM process is the surface specific energy (E_s — J/mm^2) irradiated by the laser on the powder bed, defined as

$$E_s = \frac{P}{v \cdot d}$$

where d is the diameter of the focalized laser beam (mm). This parameter was also taken into account during the results' discussion since it significantly affected the processability of the H13 powder.

For each build job, 5 different combinations of process parameters and 3 repetitions each (see Fig. 2b) were realized for a total of 15 3D bulk geometries for each plate. Samples' positioning was designed to ensure a minimum 30 mm distance between each realized geometry. Sample manufacturing was performed using 200 $^\circ\text{C}$ substrate preheating. Each layer was filled using a 5 mm width *stripe* building strategy (see Fig. 2c, d, e), changing the raster angle layer by layer according to the following sequence: 10 $^\circ$, 135 $^\circ$, 200 $^\circ$, 306 $^\circ$, 45 $^\circ$, 170 $^\circ$, 215 $^\circ$, and 345 $^\circ$. The building strategy and the raster angles were selected considering anisotropic studies founded in SLM literature, aiming to reduce the residual stresses inside the manufactured samples [32, 33].

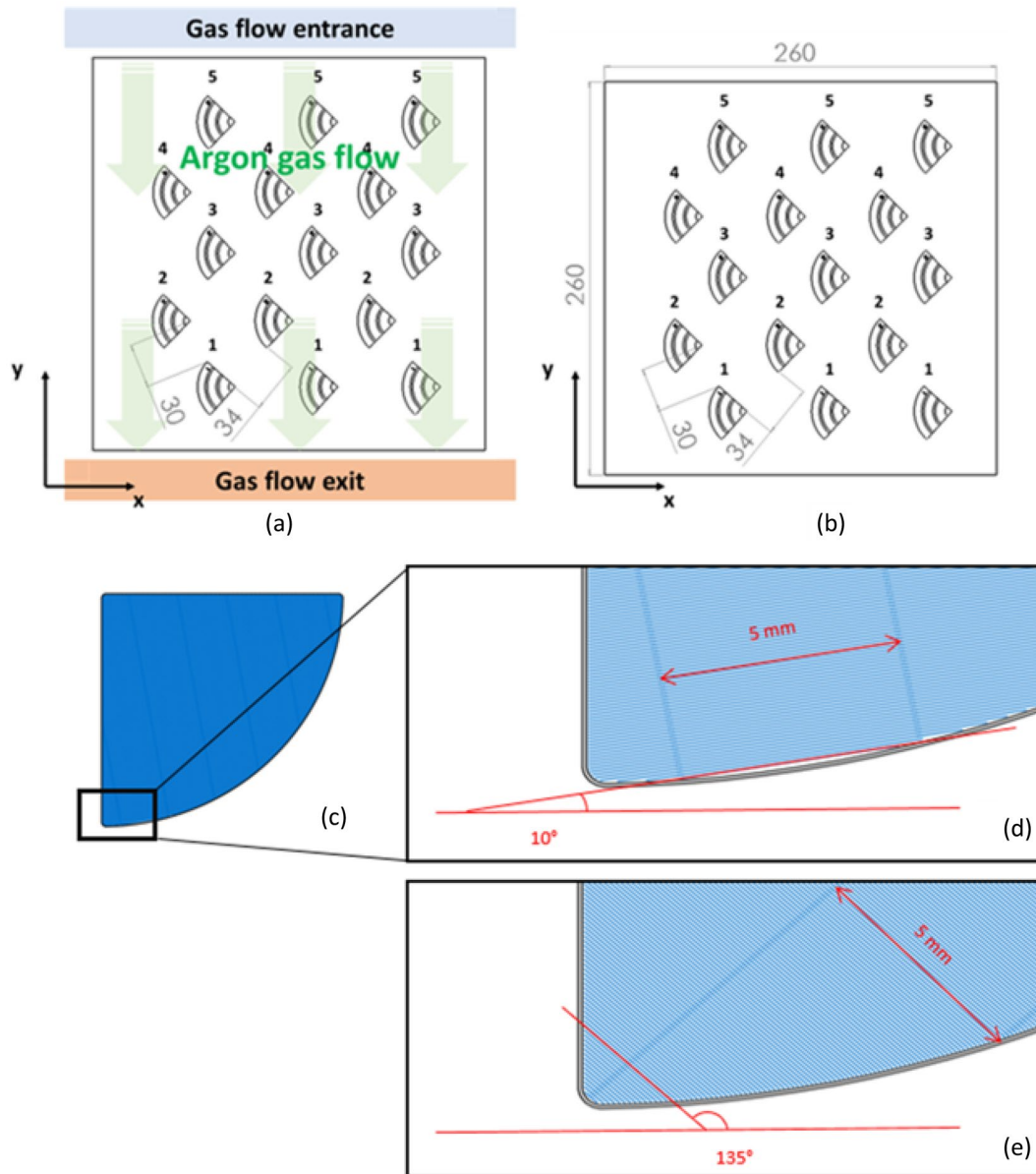


Fig. 2 **a** Shielding Argon gas flow direction; **b** arrangements of samples on the first building plate [mm]; **c** *Stripes* hatch strategy for layer infill. In particular, the first layer's infill angle of 10° **d** and the second layer's infill angle of 135° **e** are shown

Table 3 H13 printing parameters matrix. Involved VED (J/mm^3) for each parameters' combination

	P [W]	150			225			300		
		80	100	120	80	100	120	80	100	120
v [mm/s]	500	125.0	100.0	83.3	187.5	150.0	125.0	250.0	200.0	166.7
	750	83.3	66.7	55.6	125.0	100.0	83.3	166.7	133.3	111.1
	1000	62.5	50.0	41.7	93.8	75.0	62.5	125.0	100.0	83.3

Six AISI 316L plates for a total of 81 samples were used to complete the experimental campaign (5 full and 1 half-full plates, see Fig. 3). No support structures were designed for the manufacturing of the bulk geometries to

characterize the influence of the evaluated process parameters on the final quality of self-supporting geometrical features.

plate 1						plate 2					
Combination n°	P [W]	v [mm/s]	h [μm]	E _s [J/mm ²]	VED [J/mm ³]	Combination n°	P [W]	v [mm/s]	h [μm]	E _s [J/mm ²]	VED [J/mm ³]
1	150	500	80	4.3	125.0	6	300	1000	100	4.3	100.0
2	300	1000	80	4.3	125.0	7	300	1000	120	4.3	83.3
3	225	750	80	4.3	125.0	8	225	750	120	4.3	83.3
4	225	750	100	4.3	100.0	9	150	500	120	4.3	83.3
5	150	500	100	4.3	100.0	10	150	750	80	2.9	83.3
plate 3						plate 4					
Combination n°	P [W]	v [mm/s]	h [μm]	E _s [J/mm ²]	VED [J/mm ³]	Combination n°	P [W]	v [mm/s]	h [μm]	E _s [J/mm ²]	VED [J/mm ³]
11	225	1000	80	3.2	93.8	16	225	500	100	6.4	150.0
12	225	1000	100	3.2	75.0	17	225	500	120	6.4	125.0
13	225	1000	120	3.2	62.5	18	150	750	120	2.9	55.6
14	150	750	100	2.9	66.7	19	150	1000	100	2.1	50.0
15	150	1000	80	2.1	62.5	20	150	1000	120	2.1	41.7
plate 5						plate 6					
Combination n°	P [W]	v [mm/s]	h [μm]	E _s [J/mm ²]	VED [J/mm ³]	Combination n°	P [W]	v [mm/s]	h [μm]	E _s [J/mm ²]	VED [J/mm ³]
21	300	500	80	8.6	250.0	26	300	750	100	5.7	133.3
22	300	500	100	8.6	200.0	27	300	750	120	5.7	111.1
23	300	500	120	8.6	166.7						
24	300	750	80	5.7	166.7						
25	225	500	80	6.4	187.5						

Fig. 3 Combinations of process parameters for each realized job

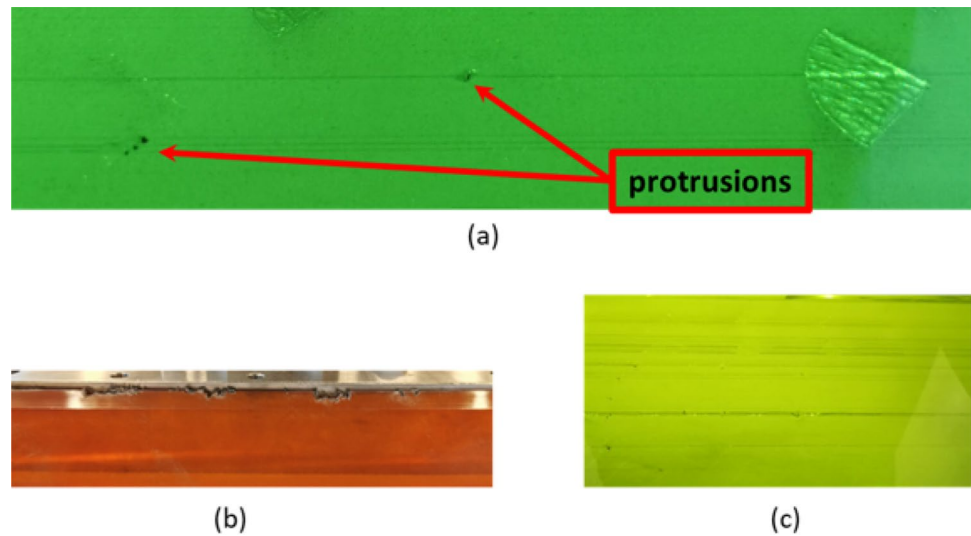
2.3 Methods analysis

The overall sample quality was assessed following two screening criteria to both evaluate the influence of the process parameters on the final quality of the realized specimens and assess the capabilities of the SLM system in printing geometrically complex AISI H13 features.

First screening step: the process status was monitored by visual observations to identify detrimental defects formed during part fabrication, such as protrusions (i.e., metallic material accumulated on the layer borders, exceeding the height of the powder bed and inducing an uneven layer growth—see Fig. 4a), which compromised the building process by colliding the polymeric wiper of the recoater during the spreading of fresh powder. Indeed, repeated impacts between metallic protrusions and the recoater cause local notching of the polymeric wiper (see Fig. 4b), leading to an uneven powder bed formation when a new layer is being formed and affecting the fabrication of the other specimens located on the building area (see Fig. 4c). Once a collision was visually detected by the machine operator (no online monitoring systems were used in this research work), the fabrication of the pertaining faulty parts was aborted.

Second screening step: the samples that successfully finished printing were detached 5 mm from the base-plate through a double vertical column band saw and an optical characterization of the samples' cross-sections was performed to assess the final achieved geometrical accuracy and internal structural integrity. Cross-section preparation was performed on the sample surface marked by the yellow arrow in Fig. 1a by a face milling operation followed by polishing to remove the typical staircase morphology of the SLM process. Image acquisition was performed through a RH 2000 digital microscope (Hirox, Tokyo, Japan) and the auto-count function tool integrated in the microscope software was used for porosity analysis, setting an investigation area of 8.5×3.5 mm. Internal cracks assessment and overhang measurements in terms of achieved sloping angle were performed by means of the open-source ImageJ software (U. S. National Institutes of Health, Maryland, USA). Each sample was coded as *laser power_scan speed_hatching distance* (i.e., Test 500_225_80 refers to the bulk geometry obtained imposing 500 W laser power, 225 mm/s scan speed, and 80 μm hatching distance). Cross-section analysis was performed according to the zones defined in Fig. 1a. The authors

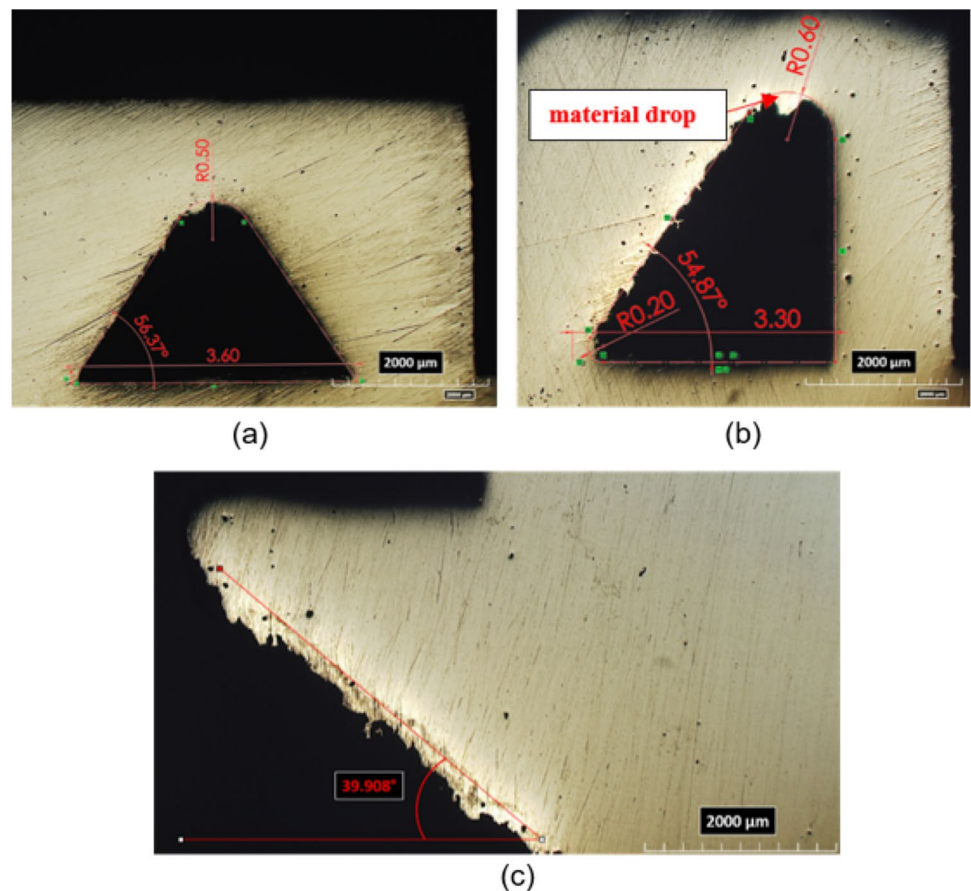
Fig. 4 **a** Protrusions' formation; **b** notched polymeric wiper due to protrusions' formation; **c** uneven powder bed formation due to wiper's notching



first investigated the zone 4 to assess the capability of the SLM process in realizing internal cavity and unsupported geometries, comparing the obtained features with the nominal ones (see Fig. 5a, b), then they focused on zone 3 to characterize the quality of overhanging structures (see Fig. 5c), measuring the achieved sloping angle.

Finally, the analysis of the internal quality of zones 1 and 2 in terms of pores (see Fig. 6), lack of fusion, cracks, and delamination was performed.

Fig. 5 Geometry assessment by means of optical analysis: (a) zone 4—isosceles triangle, test 150_750_100; (b) zone 4—rectangular triangle, test 150_500_100; (c) zone 3—nominal 35° overhang, test 225_750_100. Dimension in millimeters



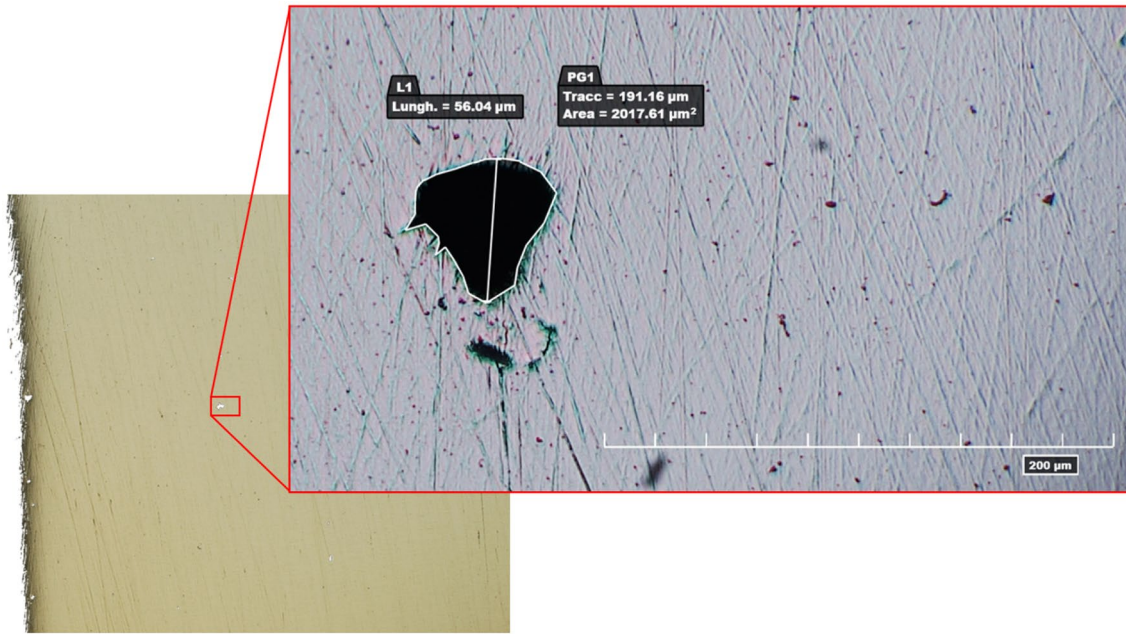


Fig. 6 Porosity assessment of sample 150_750_80 in zone 1: quantifying pore areas to determine porosity percentage. In addition, maximum pore length is reported for comprehensive analysis

3 Results

The results are reported according to the screening criteria introduced in the materials and methods section. During the first screening step (i.e., the visual observation of the process status), the printing of all the samples involving 300 W laser power and of six specimens fabricated at 225 W was stopped due to the formation of strong protrusions along the sample contours (see Table 4). In addition, the process combination involving $P = 150$ W, $v = 500$ mm/s, and $h = 80$ μm failed, exhibiting building defects in the infill area of the realized layers of zone 1 of the designed sample geometry (see Fig. 1a). Figure 7a shows the observed defects occurring during the manufacturing of test 150_500_80, while protrusions occurring for 300 W are shown in Fig. 7b. Table 4 shows the samples successfully printed and the ones interrupted. At the end of the experimental campaign, 33 out of 81 H13 samples were entirely produced without any evidence of protrusions (see Fig. 7c).

The second screening step was focused on the inspection of the internal quality of the successfully realized parts starting from zone 4 to zone 1. The performed analysis highlighted the presence of three categories of defects:

- (1) high porosity in the core of zone 3 and 4 (see Fig. 8a);
 - (2) contour defect in overhanging structure of zone 3 and in internal channel of zone 4 (see Fig. 8b);
 - (3) material drops or jagged profiles at the vertical fillet radii (see Fig. 8c).
- (1) Zones 1 and 2 exhibited a lower porosity (i.e., 0.11% and 0.09% on average, respectively) compared to zones 3 and 4 (i.e., 0.15% and 0.51% on average, respectively). Pores sizes vary in a range of 60–130 μm in zone 3 and 4 and between 45 and 70 μm in zone 1 and 2 in accordance with research findings discussed in the literature [34–36]. The lower porosity was obtained for tests 150_500_120, 150_1000_80, and 150_1000_100, showing an average internal density ranging between 99.91% and 99.93%. Table 5 and Fig. 9 summarizes

Table 4 Results of the first screening step: = ✓ part completely produced, = × interrupted part production, Z# = failure zone

	P [W]	150			225			300		
		h [μm]	80	100	120	80	100	120	80	100
v [mm/s]	500	× Z1	✓	✓	× Z1	✓	✓	× Z1	× Z1	× Z1
	750	✓	✓	✓	× Z1	✓	× Z1	× Z1	× Z1	× Z1
	1000	✓	✓	✓	× Z3	× Z3	× Z1	× Z1	× Z1	× Z1

Fig. 7 **a** Defect formation during and after SLM production—test 150_500_80; **b** failed sample for 300 W; **c** successfully printed H13 samples

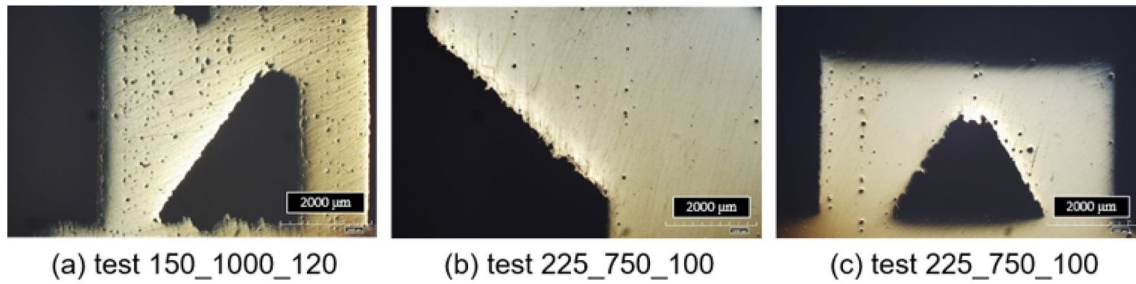
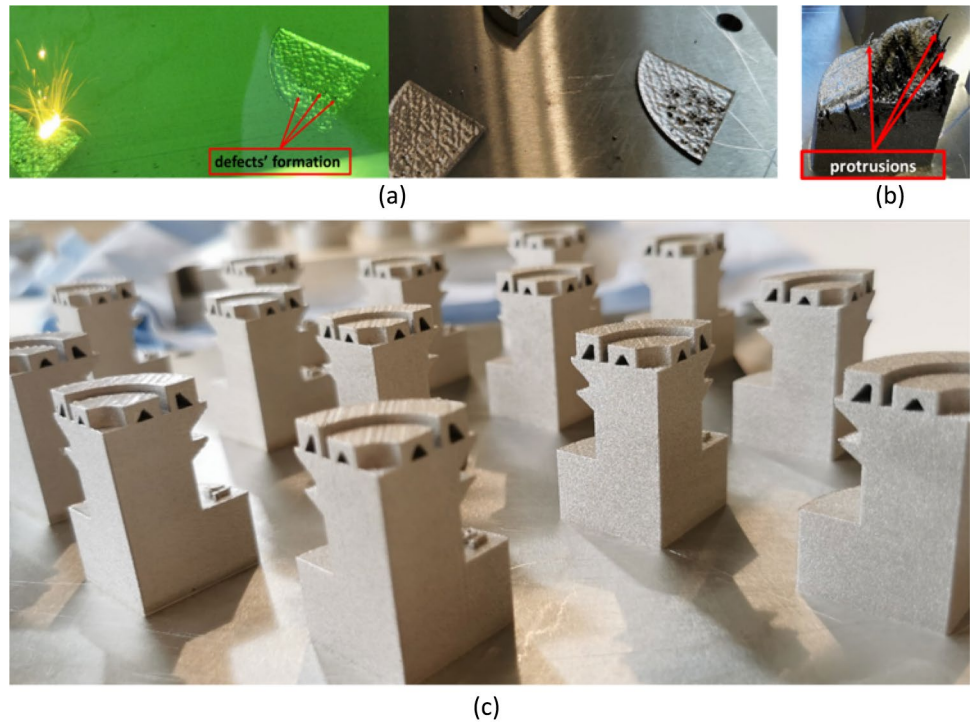
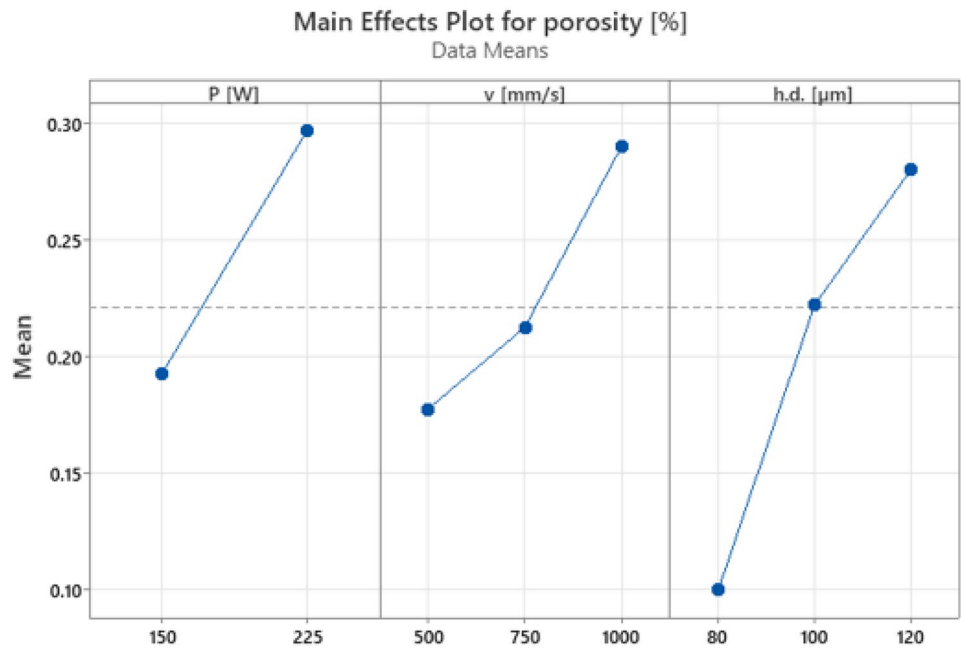


Fig. 8 Main observed defects: **(a)** porosity, **(b)** jagged edges, **(c)** material drop

Table 5 Detected porosity for each successfully realized sample

combo n°	P [W]	v [mm/s]	h.d. [μm]	E_s [J/mm ²]	VED [J/mm ³]	porosity [%]	max pore length [μm]
4	225	750	100	4.3	100.0	0.43	135.00
5	150	500	100	4.3	100.0	0.17	117.00
9	150	500	120	4.3	83.3	0.08	78.00
10	150	750	80	2.9	83.3	0.11	83.00
14	150	750	100	2.9	66.7	0.15	114.00
15	150	1000	80	2.1	62.5	0.09	84.00
16	225	500	100	6.4	150.0	0.27	176.00
17	225	500	120	6.4	125.0	0.19	89.00
18	150	750	120	2.9	55.6	0.16	102.00
19	150	1000	100	2.1	50.0	0.09	69.00
20	150	1000	120	2.1	41.7	0.69	104.00

Fig. 9 Main effective plot of internal porosity



the detected internal porosity for each analyzed sample zone.

- (2) The measured overhang angles varied between +4.91° and -0.78°, and between +3.62° and -1.76° compared to the nominal sloping angle of 35° and 40°, respectively. In particular, for 225 W laser power, the nominal 35° inclined surfaces exhibited significant material drops along the downskin, which degraded the geometrical accuracy of the realized part (see Figs. 5c, 8b).
- (3) The cross-sections of the analyzed internal channels revealed significant material drops at the vertical fillet radii when medium laser energies were employed, observing a general jagged profile for each characterized process condition (see Fig. 5b, 8c).

Table 6 summarizes the experimental results in terms of measured overhang angle and geometrical quality of the vertical fillet radius of the realized cross-sections of the internal channels.

The experimental investigation reported in Table 6 showed that the combinations of process parameters involving 225 W resulted in the largest and in the smallest dimensional deviations of the measured inclined angle (i.e., test 225_750_100 showed a measured angle deviation of +4.91° and +3.62° for 35° and 40°, respectively, while test 225_500_120 showed a measured angle deviation of -0.51° and +0.09). Nevertheless, for both cases, a high degradation of the part edges in terms of material drops and jagged

Table 6 Measured overhang angles and geometrical quality of the upper side of internal feature.

Combo n°	P [W]	v [mm/s]	h.d. [μm]	E _s [J/mm ²]	VED [J/mm ³]	Deviation from 35° nominal	Deviation from 40° nominal	Material drop	Jagged edges
4	225	750	100	4.3	100.0	+4.91	+3.62	✓	✓
5	150	500	100	4.3	100.0	+2.38	+3.06	✓	-
9	150	500	120	4.3	83.3	+4.34	-1.76	✓	✓
10	150	750	80	2.9	83.3	+2.54	-0.13	✓	✓
14	150	750	100	2.9	66.7	+1.47	-0.31	-	✓
15	150	1000	80	2.1	62.5	-0.78	-1.30	✓	✓
16	225	500	100	6.4	150.0	+2.74	-0.66	✓	-
17	225	500	120	6.4	125.0	-0.51	+0.09	✓	✓
18	150	750	120	2.9	55.6	+1.34	+1.89	✓	✓
19	150	1000	100	2.1	50.0	+0.23	-0.90	✓	✓
20	150	1000	120	2.1	41.7	+1.92	-0.59	-	✓

✓: defect observed; -: no defects

edges was detected. On the contrary, using low laser power limited the formation of geometrical defects, increasing the overall quality of the realized samples. However, for energy densities ranging between 83.3 and 150 J/mm^3 , strong deviations of the overhang angle were observed even for 150 W . The cross-sections of the inner channels generally showed a $100 \text{ }\mu\text{m}$ – $300 \text{ }\mu\text{m}$ material collapse at the vertical fillet radii followed by indented edges. Figure 10 reports micrographs sections of test 150_1000_80 and 150_1000_100 as a function of the designed zones.

4 Discussion

Considering the results of the first screening step reported in Table 4, the reason for the building failure was the fusion/combustion debris accumulated on the border of the samples, resulting in thick solidified protrusions (see Figs. 10b and 11a), combined with a significant particle spattering occurring at high laser power, that contaminated the surrounding powder bed due to a considerable ejection of molten material (see Fig. 12a). The formation of solidified protrusions damaged the polymeric wiper of the recoater and it was no longer possible to properly cover the building plate with fresh H13 powder (see Fig. 4b). This kind of defect was observed for all the combinations of process parameters involving high laser power

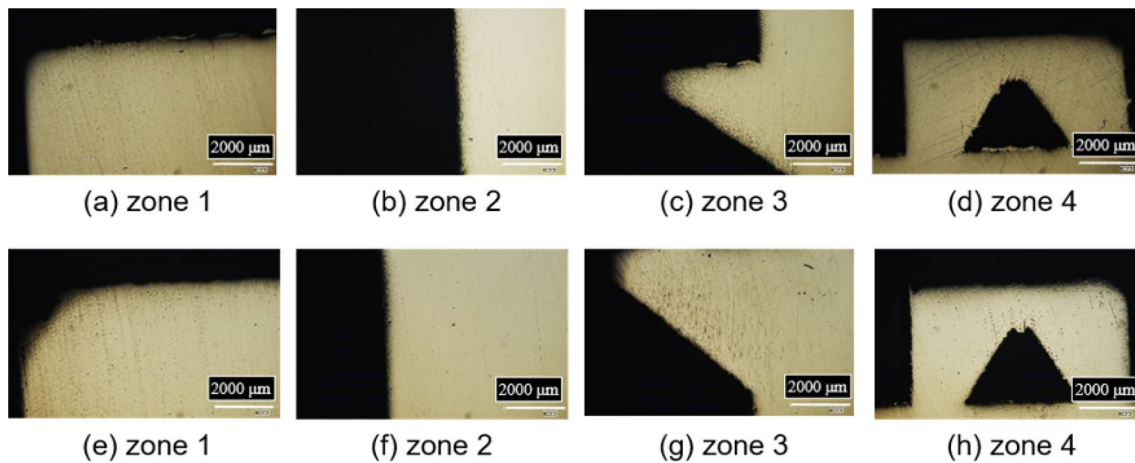


Fig. 10 Main section micrographs: (a–d) test 150_1000_80 and (e–h) test 150_1000_100

Fig. 11 Examples of failures: (a) in zone 1 for the test 300_1000_100, (b) in zone 3 for the test 225_1000_100

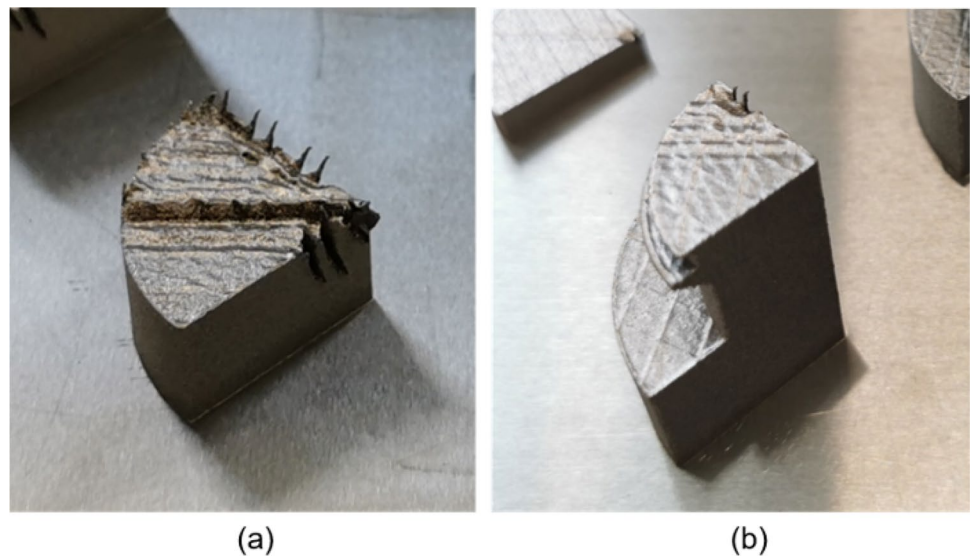
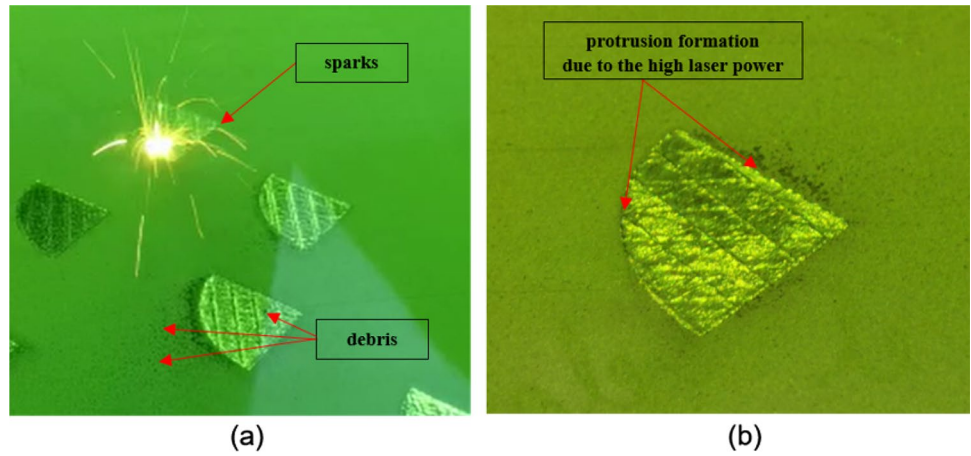


Fig. 12 **a** Examples of deposition of particles from an irradiated area on already built layers and on the powder bed, **b** starting of protrusion formation due to the high laser power for the test 300_1000_80



(i.e., 300 W—see Fig. 12a) as confirmed by Narvan et al. [15] which demonstrated protrusions’ formation for high VED. Moreover, the intense sparks and combustion debris occurring at 300 W compromised the fabrication of test samples located in their proximity, which involved lower laser power (i.e., 225 W and 150 W) and medium–low VED ranging between 125 and 62.5 J/mm³. The strong contamination and quality degradation of the powder bed surrounding 300 W test samples forced to interrupt the fabrication of tests 1 (see Fig. 7a), 3, 8, and 25 (see Fig. 3) due to defects’ formation induced by spattering and the impact of protrusion with the recoater wiper (see Fig. 3 and Table 4). In addition, the realization of tests 11, 12, and 13 involving 225 W and a scan speed of 1000 mm/min/s was interrupted due to protrusion formation that mainly occurred in zone 3 (see Fig. 12b). At the moment of article writing, the reason for the occurrence of this phenomenon for these last three samples (11, 12, and 13) is hardly explainable and further analysis is required. The authors have planned to repeat the test samples involving a laser power of 225 W to avoid the influence of particle spattering occurring at 300 W during sample manufacturing and deeply characterize the correlation between the SLM process parameters and the protrusion formation for a laser power of 225 W.

On the contrary, the printing of test samples involving a laser power of 150 W was successfully completed. The lower value of the laser power limited the formation of sparks and

dense fumes, preventing the detrimental contamination of the powder bed and enabling the complete printing of the samples.

The internal analysis performed on the successful as-built samples confirmed the previous investigation concerning the detrimental influence of intense fumes and sparks on the structural quality of the realized part. All the samples involving 225 W exhibited a marked internal porosity increasing with sample height. The worst case was the test 225_750_100 showing an internal density that decreased from 99.73% to 99.35% moving from Zone 1 to Zone 4 (see Table 7). On the contrary, H13 samples fabricated at low laser power showed a higher internal density with a more homogeneous pore distribution. The performed internal analysis highlighted the importance to limit the formation of fumes and sparks during the SLM manufacturing of H13 samples, underlining the significance of optimizing SLM process parameters to reduce the powder bed contamination and increase process quality. For this reason, the authors chose to perform the following analyses focusing on the observed geometrical and internal quality of the as-built samples realized at 150 W, neglecting the tests performed at 225 W due to the poor detected structural quality.

Except for test 150_500_80, which failed due to its proximity to the sample manufactured at 300 W, all the as-built H13 samples realized at 150 W showed an internal density higher than 99.00%, exhibiting an internal porosity ranging between 0.08% and 0.69% (see Table 5). This result

Table 7 Porosity distribution along the four sample zones

Combo n°	P [W]	v [mm/s]	h.d [um]	E _s [J/mm ²]	VED [J/mm ³]	Zone 4 [%]	Zone 3 [%]	Zone 2 [%]	Zone 1 [%]
4	225	750	100	4.3	100.0	0.65	0.48	0.30	0.27
16	225	500	100	6.4	150.0	0.61	0.18	0.10	0.17
17	225	500	120	6.4	125.0	0.40	0.16	0.06	0.12

demonstrated that, for the evaluated experimental range, the employment of low levels for the laser power enabled the fabrication of dense H13 samples also for VED ranging between 50 and 100 J/mm³ and E_s ranging between 2.1 and 4.3 J/mm². On the contrary, the lowest level of VED (i.e., 41.7 J/mm³) in conjunction with the lowest level of E_s (i.e., 2.1 J/mm²) did not ensure a full melt pool formation resulting in a high number of lack of fusions which degraded the internal density of the part, increasing the internal porosity up to 0.69%. This outcome was deeply explained by [15, 36] and it is mainly related to the increase of the laser speed that, for constant laser power, results in insufficient energy input to properly melt the powder particles, with a consequent lack of fusion between layers. The presence of irregular pores due to lack of fusion reduces both the resistance to failure and the ductility of as-built SLM parts as demonstrated in [37]. For this reason, combinations of process parameters resulting in lacks of fusions should be avoided in the manufacturing of metallic components by SLM.

Considering the milling tool component presented by the authors in [23] and from which the sample geometry was designed, acceptable densities for application range between 99.80% and 99.99%. In our work, the majority of the realized samples exhibited an internal density higher than 99.80% (e.g., the lower internal porosity of 0.08% was achieved by test 150_500_120). However, all the completed samples are currently undergoing stress relief and HIP treatments that could improve the internal density of samples 4, 16, and 20 (see Table 5). A second work will reconsider all the porosity measurements post-heat treatments for all the processed samples.

Low geometrical deviations from the nominal 35° overhang angle were obtained for VED ranging between 50 and 62.5 J/mm³. For VED higher than 62.5 J/mm³, an increase in the dimensional deviation was observed. In particular, for VED ranging between 83.3 and 100 J/mm³, a strong degradation of the edges' accuracy was observed, detecting a significant material drops along the downskin side of the inclined surface. The reason of such behavior was mainly related to the input energy involved in powder melting and melt pool cooling rate. High VED increases the size and the temperature of the melt pool, reducing both the viscosity and the cooling rate of the molten material which drops downwards due to the gravity force, not being able of self-supporting. At constant VED, this phenomenon was amplified for high E_s , causing dimensional deviations up to +4.34°. On the contrary, for 41.7 J/mm³ the process was unable to properly reproduce the designed overhang due to the high presence of lack of fusions which compromises the integrity of the parts' edges and feature profile. Compared to the nominal 35° overhang, for the nominal 40° overhang, dimensional deviations lower than 2° were achieved for a

wider range of VED, detecting a strong geometry degradation only for test 150_500_100, which involved a VED of 100 J/mm³.

Larger deviations from the nominal dimensions were obtained for the cross-sections of the internal channels. Contrary to the realized overhang, defects such as material drop or jagged edges were observed for all the evaluated combinations of process parameters (see Fig. 10). Specifically, the dimension of the material collapse detected at the vertical fillet radii increased with the involved laser power and VED, reaching a maximum length of 300 µm. Nevertheless, for low laser power (150 W) and medium–high hatching distance (80–100 µm), acceptable results were obtained. These results provided an indication on the capabilities of the SLM process in manufacturing self-supported features.

5 Conclusion

A structured experimental campaign was conducted to establish a set of process parameters suitable for the SLM additive manufacturing of H13 tool steel powder. Sample geometries were designed based on the dimensions and the geometric features of a milling tool previously presented by the authors: two overhanging surfaces with different slopes (35° and 40°) and internal channels with different triangular cross-sections and vertical fillet radii between 0.5 and 0.6 mm.

The experimental campaign highlighted the importance to limit the formation of fumes and sparks during SLM process optimization of H13 tool steel powder to reduce the powder bed contamination, prevent protrusion formation, and increase process quality. In particular, a laser power equal to 150 W ensured high internal quality in terms of porosity homogeneity reaching an 99.9% internal density. Among these combinations, medium–low values of VED (<65 J/mm³) and E_s (<3 J/mm²) resulted in low geometrical deviations from the nominal overhang angles with limited material drop, increasing the final geometrical accuracy of the realized H13 parts. However, the lowest level of VED (41.7 J/mm³) in conjunction with the lowest level of E_s (2.1 J/mm²) resulted in a high number of lack of fusions.

Finally, the experimental outcomes underlined that high-quality H13 parts exhibiting high internal density and low deviations from the nominal design are feasible by means of an adaptation of the SLM process parameters based on both the geometrical shape and requirements of the part to be realized. In particular, with regard to the evaluated experimental range, H13 samples showing an internal density of 99.92% and a low geometrical deviation of +0.23° and –0.90° of the measured 35° and 40° sloping angle, respectively, can be achieved involving 150 W, 500 mm/s,

and 120 μm for the layer infill in conjunction with 150 W, 1000 mm/s, and 100 μm for the layer contour.

The fabricated samples are currently undergoing a sequence of heat treatments (such as stress relieving and HIP) to analyze the evolution of residual stresses and microstructure behavior as a function of the treatment temperature profile and have a final porosity and geometry evaluation, comparing the results obtained pre- and post-heat treatments. The analysis will integrate the results reported in this work to finally select a suitable process parameters combination for the SLM manufacturing of H13 tools. The exploitation of these results for defect classification and parameter analysis will provide valuable insights into the intricacies of the observed defects, contributing in future research works to get targeted and efficient approaches to monitoring and control. Furthermore, these findings will be helpful in validating numerical models for SLM.

Acknowledgements The authors would like to thank Schneider Tools, Kind Special Alloy and Prima Power, who sponsored and supported the research. The authors would like to mention that the present work has been carried out in the framework of the AITeM-PromozioneL@ser association.

Author contributions All the authors contributed to the study conception and design, with active participation in material preparation, data collection and analysis. The manuscript was iteratively written and revised by all the authors. All the authors read and approved the final manuscript.

Funding Open access funding provided by SUPSI - University of Applied Sciences and Arts of Southern Switzerland.

Data availability The authors declare that the data supporting the findings of this study are available within the paper. Supplementary information can be requested from the corresponding author.

Declarations

Conflict of interest All the authors certify that they have no affiliations with or involvement in any organization or entity with any financial interest or non-financial interest in the subject matter or materials discussed in this manuscript.

Open Access This article is licensed under a Creative Commons Attribution 4.0 International License, which permits use, sharing, adaptation, distribution and reproduction in any medium or format, as long as you give appropriate credit to the original author(s) and the source, provide a link to the Creative Commons licence, and indicate if changes were made. The images or other third party material in this article are included in the article's Creative Commons licence, unless indicated otherwise in a credit line to the material. If material is not included in the article's Creative Commons licence and your intended use is not permitted by statutory regulation or exceeds the permitted use, you will need to obtain permission directly from the copyright holder. To view a copy of this licence, visit <http://creativecommons.org/licenses/by/4.0/>.

References

- Frazier WE (2014) Metal additive manufacturing: a review. *J Mater Eng Perform* 23(6):1917–1928. <https://doi.org/10.1007/s11665-014-0958-z>
- DebRoy T, Wei HL, Zuback JS, Mukherjee T, Elmer JW, Milewski JO, Beese AM, Wilson-Heid A, De A, Zhang W (2018) Additive manufacturing of metallic components. *Process Struct Properties Progress Mater Sci* 92:112–224. <https://doi.org/10.1016/j.pmatsci.2017.10.001>
- Ngo TD, Kashani A, Imbalzano G, Nguyen KTQ, Hui D (2018) Additive manufacturing (3D printing): A review of materials, methods, applications and challenges. *Compos B Eng* 143:172–196. <https://doi.org/10.1016/j.compositesb.2018.02.012>
- Gu DD, Meiners W, Wissenbach K, Poprawe R (2012) Laser additive manufacturing of metallic components: Materials, processes and mechanisms. *Int Mater Rev* 57(3):133–164. <https://doi.org/10.1179/1743280411Y.0000000014>
- Herzog D, Seyda V, Wycisk E, Emmelmann C (2016) Additive manufacturing of metals. *Acta Mater* 117:371–392. <https://doi.org/10.1016/j.actamat.2016.07.019>
- Gao W, Zhang Y, Ramanujan D, Ramani K, Chen Y, Williams CB, Wang CCL, Shin YC, Zhang S, Zavattieri PD (2015) The status, challenges, and future of additive manufacturing in engineering CAD. *Comput Aided Design* 69:65–89. <https://doi.org/10.1016/j.cad.2015.04.001>
- Sames WJ, List FA, Pannala S, Dehoff RR, Babu SS (2016) The metallurgy and processing science of metal additive manufacturing. *Int Mater Rev* 61(5):315–360. <https://doi.org/10.1080/09506608.2015.1116649>
- ASM International Handbook Committee (1990) Properties and selection: irons, steels, and high-performance alloys. In: *Metals handbook*, vol 1, 10th edn.
- Hanzl P, Zetková I (2019) Benefits of a new approach to designing milling cutter using metal additive manufacturing. *Manuf Technol* 19(3):385–390. <https://doi.org/10.21062/ujep/301.2019/a/1213-2489/mt/19/3/385>
- Laakso P, Riipinen T, Laukkanen A, Andersson T, Jokinen A, Revuelta A, Ruusuuvuori K (2016) Optimization and simulation of SLM process for high density H13 tool steel parts. *Phys Proc* 83:26–35. <https://doi.org/10.1016/j.phpro.2016.08.004>
- Fonseca EB, Gabriel AHG, Araújo LC, Santos PLL, Campo KN, Lopes ESN (2020) Assessment of laser power and scan speed influence on microstructural features and consolidation of AISI H13 tool steel processed by additive manufacturing. *Addit Manuf* 34:10125. <https://doi.org/10.1016/j.addma.2020.101250>
- Katancik M, Mirzababaei S, Ghayoor M, Pasebani S (2020) Selective laser melting and tempering of H13 tool steel for rapid tooling applications. *J Alloys Compounds* 849:156319. <https://doi.org/10.1016/j.jallcom.2020.156319>
- Yan JJ, Zheng DL, Li HX, Jia X, Sun JF, Li YL, Qian M, Yan M (2017) Selective laser melting of H13: microstructure and residual stress. *J Mater Sci* 52(20):12476–12485. <https://doi.org/10.1007/s10853-017-1380-3>
- Kurzynowski T, Stopyra W, Gruber K, Ziólkowski G, Kuznicka B, Chlebus E (2019) Effect of scanning and support strategies on relative density of SLM-ed H13 steel in relation to specimen size. *Materials* 12(2):239. <https://doi.org/10.3390/ma12020239>
- Narvan M, Al-Rubaie KS, Elbestawi M (2019) Process-structure-property relationships of AISI H13 tool steel processed with selective laser melting. *Materials* 12(14):2284. <https://doi.org/10.3390/ma12142284>
- Wang M, Li W, Wu Y, Li S, Cai C, Wen S, Wei Q, Shi Y, Ye F, Chen Z (2019) High-temperature properties and microstructural stability of the AISI H13 hot-work tool steel processed by

- selective laser melting. *Metall Mater Trans B* 50(1):531–542. <https://doi.org/10.1007/s11663-018-1442-1>
17. Malekipour E, El-Mounayri H (2018) Common defects and contributing parameters in powder bed fusion AM process and their classification for online monitoring and control: a review. *Int J Adv Manuf Technol* 95:527–550. <https://doi.org/10.1007/s00170-017-1172-6>
 18. Afrasiabi M, Keller D, Lüthi C, Bambach M, Wegener K (2022) Effect of process parameters on melt pool geometry in laser powder bed fusion of metals: a numerical investigation. *Proc CIRP* 113:378–384. <https://doi.org/10.1016/j.procir.2022.09.187>
 19. Wang X, Keya T, Chou K (2016) Build Height effect on the inconel 718 parts fabricated by selective laser melting. *Proc Manuf* 5:1006–1017. <https://doi.org/10.1016/j.promfg.2016.08.089>
 20. Yao Y, Wang K, Wang X, Li L, Cai W, Kelly S, Yan F (2020) Microstructural heterogeneity and mechanical anisotropy of 18Ni-330 maraging steel fabricated by selective laser melting: the effect of build orientation and height. *J Mater Res* 35(15):2065–2076. <https://doi.org/10.1557/jmr.2020.126>
 21. Kučerová L, Zetková I (2016) Metallography of 3D printed 1.2709 tool steel. *Manuf Technol* 16 (1):140–144. <https://doi.org/10.21062/UJEP/301.2019/A/1213-2489/MT/19/3/385>
 22. Syam WP, Jianwei W, Zhao B, Maskery I, Elmadih W, Leach R (2018) Design and analysis of strut-based lattice structures for vibration isolation. *Precis Eng* 52:494–506. <https://doi.org/10.1016/j.precisioneng.2017.09.010>
 23. Tomasoni D, Giorleo L, Ceretti E (2021) Milling tool optimization by topology optimization technique. *ESAFORM 2021—24th International Conference on Material Forming* 3972. <https://doi.org/10.25518/esaform21.3972>
 24. Sing SL, An J, Yeong WY, Wiria FE (2016) Laser and electron-beam powder-bed additive manufacturing of metallic implants: a review on processes, materials and designs. *J Orthop Res* 34(3):369–385. <https://doi.org/10.1002/jor.23075>
 25. Qian X (2017) Undercut and overhang angle control in topology optimization: a density gradient based integral approach. *Int J Numer Meth Eng* 111(3):247–272. <https://doi.org/10.1002/nme.5461>
 26. Allaire G, Dapogny C, Estevez R, Faure A, Michailidis G (2017) Structural optimization under overhang constraints imposed by additive manufacturing technologies. *J Comput Phys* 351:295–328. <https://doi.org/10.1016/j.jcp.2017.09.041>
 27. Guo X, Zhou J, Zhang W, Du Z, Liu C, Liu Y (2017) Self-supporting structure design in additive manufacturing through explicit topology optimization. *Comput Methods Appl Mech Eng* 323:27–63. <https://doi.org/10.1016/j.cma.2017.05.003>
 28. Li Q, Chen W, Liu S, Tong L (2016) Structural topology optimization considering connectivity constraint. *Struct Multidiscip Optim* 54(4):971–984. <https://doi.org/10.1007/s00158-016-1459-5>
 29. ASTM B822–20 (2020) Standard test method for particle size distribution of metal powders and related compounds by light scattering
 30. ASTM E1019–18 (2018) Standard Test Methods for Determination of Carbon, Sulfur, Nitrogen, and Oxygen in Steel, Iron, Nickel, and Cobalt Alloys by Various Combustion and Inert Gas Fusion Techniques
 31. ASTM E1479–16 (2016) Standard Practice for Describing and Specifying Inductively Coupled Plasma Atomic Emission Spectrometers
 32. Huang W, Chen X, Huang X et al (2021) Anisotropic study of Ti6Al4V alloy formed by selective laser melting. *JOM* 73:3804–3811. <https://doi.org/10.1007/s11837-021-04765-0>
 33. Rajendran VRK, Mamidi K, Ravichander B, Farhang B, Amerinanzani A, Moghaddam S (2020) Determination of residual stress for Inconel 718 samples fabricated through different scanning strategies in selective laser melting. *Behav Mech Multifunctional Mater* 9:1137719. <https://doi.org/10.1117/12.2558342>
 34. Prashanth KG, Eckert J (2017) Formation of metastable cellular microstructures in selective laser melted alloys. *J Alloy Compd* 707:27–34. <https://doi.org/10.1016/j.jallcom.2016.12.209>
 35. Röttger A, Boes J, Theisen W, Thiele M, Esen C, Edelmann A, Hellmann R (2020) Microstructure and mechanical properties of 316L austenitic stainless steel processed by different SLM devices. *Int J Adv Manuf Technol* 108(3):769–783. <https://doi.org/10.1007/s00170-020-05371-1>
 36. Wang J, Liu S, Fang Y, He Z (2020) A short review on selective laser melting of H13 steel. *Int J Adv Manuf Technol* 108:2453–2466. <https://doi.org/10.1007/s00170-020-05584-4>
 37. Plessis A, Yadroitsava I, Yadroitsev I (2020) Effects of defects on mechanical properties in metal additive manufacturing: a review focusing on X-ray tomography insights. *Mater Design* 187:108385. <https://doi.org/10.1016/j.matdes.2019.108385>

Publisher's Note Springer Nature remains neutral with regard to jurisdictional claims in published maps and institutional affiliations.